NUMERICAL INVESTIGATION OF TOROIDAL SHOCK WAVES FOCUSING USING DISCONTINUOUS GALERKIN FINITE ELEMENT METHOD

Chen Eryun[1], *Zhao Gaiping*[2], *Zhuo Wentao*[1], *Yang Ailing*[1]

(1. School of Energy and Power Engineering, University of Shanghai for Science & Technology, Shanghai, 200093, P. R. China;
2. School of Medical Instrument and Food Engineering, University of Shanghai for Science & Technology, Shanghai, 200093, P. R. China)

Abstract: A numerical simulation of the toroidal shock wave focusing in a co-axial cylindrical shock tube is investigated by using discontinuous Galerkin (DG) finite element method to solve the axisymmetric Euler equations. For validating the numerical method, the shock-tube problem with exact solution is computed, and the computed results agree well with the exact cases. Then, several cases with higher incident Mach numbers varying from 2.0 to 5.0 are simulated. Simulation results show that complicated flow-field structures of toroidal shock wave diffraction, reflection, and focusing in a co-axial cylindrical shock tube can be obtained at different incident Mach numbers and the numerical solutions appear steep gradients near the focusing point, which illustrates the DG method has higher accuracy and better resolution near the discontinuous point. Moreover, the focusing peak pressure with different grid scales is compared.

Key words: shock wave focusing; spherical double Mach reflection; discontinuous galerkin finite element method

CLC number: O354.4 **Document code**: A **Article ID**: 1005-1120(2012)01-0009-07

INTRODUCTION

Shock wave focusing has been an interesting research area for several decades. A locally high pressures and temperatures created by shock wave focusing have been applied to various interesting scientific, industrial, and medical purposes[1-2]. Experimental studies of such focusing process at low incident Mach number have been extensively investigated in the past several decades[1,3-6], which have provided valuable insight into understanding the nature of such flows. But it is usually complex, expensive and time consuming, especially for higher Mach number cases which are more interesting in physics and important in practice. As the advent of supercomputers and the sharply increasing of computational speed, the direct numerical solution of governing equations, which is less expensive, yet reliable, and especially suitable to variable flow conditions, makes even more attractive.

Sod[7] first numerically studied the focusing of cylindrical shock wave with the one dimensional model using combination of Glimm's method and operator splitting. The focusing of shock waves for incident Mach numbers ranging from 1.1 to 2.0 was experimentally investigated by Izumi[5] and compared with numerical results obtained using Piecewise Linear Method. Jiang et al[8-10] numerically estimated the peak pressures attainable in toroidal shock wave focusing using dispersion controlled dissipation (DCD) scheme. But these

Foundation items: Supported by the National Natural Science Foundation of China (50976072, 51106099, 10902070); the Leading Academic Discipline Project of Shanghai Municipal Education Commission (J50501); the Science Foundation for the Excellent Youth Scholar of Higher Education of Shanghai (slg09003).

Received date: 2011-01-10; **revision received date**: 2011-07-21

E-mail: cey168@126.com

methods usually achieve high-order accuracy by using a wide stencil, which may lose accuracy in a fairly large region near shocks.

In this paper, a discontinuous Galerkin(DG) finite element method with third-order accuracy is used to simulate the toroidal shock wave focusing in a co-axial cylindrical shock tube. The method[11-15] has several advantages including its flexibility in handling an irregular solution domain, formally uniformly high-order accurate, and the requirement of fewer adjacent grid points, which extremely provides convenience for programming and computing.

1 MATHEMATICAL MODEL

1.1 Governing equations

The governing equations are expressed by using axisymmetric Euler equations in the cylindrical coordinate system as follows

$$\frac{\partial \boldsymbol{U}}{\partial t}+\frac{\partial \boldsymbol{F}}{\partial x}+\frac{\partial \boldsymbol{G}}{\partial y}=\boldsymbol{S} \qquad (x,y)\in\Omega \tag{1}$$

where

$$\boldsymbol{U}=[\rho,\rho u,\rho v,E]^{\mathrm{T}}$$
$$\boldsymbol{F}=[\rho u,\rho u^2+p,\rho uv,(E+p)u]^{\mathrm{T}}$$
$$\boldsymbol{G}=[\rho v,\rho uv,\rho v^2+p,(E+p)v]^{\mathrm{T}}$$
$$\boldsymbol{S}=\left(\frac{-\rho v}{y}\right)\left[1,u,v,\frac{(E+p)}{\rho}\right]^{\mathrm{T}} \qquad \Omega\in\boldsymbol{R}^2$$

where t is the time, ρ the density, u and v are the velocity components along the x, y axes respectively, p is pressure, and E the total energy per unit volume

$$E=\frac{p}{\gamma-1}+\frac{\rho(u^2+v^2)}{2} \tag{2}$$

where γ is the ratio of specific heat.

1.2 Space discretization

First, Eq. (1) is discretized in space using the DG method. For $\forall\, t$, the approximate solution $\boldsymbol{U}(\boldsymbol{X},t)$ is sought in the discontinuous finite element space

$$V_h=\{v_h\in L^{\infty}(\Omega);v_h\Big|_K\in V(K),\forall\, K\in\Gamma_h\}$$

where Γ_h is the finite partition of the domain Ω and $V(K)$ the so-called local space, which is taken as the collection of polynomials of degree k. Set $k=2$ in this paper.

In order to determine the approximate solution $\boldsymbol{U}_h(\boldsymbol{X},t)$, we multiply Eq. (1) by $v_h\in V_h$, and integrate over $K\in\Gamma_h$, then replace the exact solution $\boldsymbol{U}(\boldsymbol{X},t)$ by approximation $\boldsymbol{U}_h(\boldsymbol{X},t)\in V_h$, finally use Green formulation. We obtain

$$\int_K\frac{\partial}{\partial t}\boldsymbol{U}_h(\boldsymbol{X},t)v_h(\boldsymbol{X})\mathrm{d}\Omega+\sum_{e\in\partial K}\int_e\boldsymbol{f}(\boldsymbol{U}_h(\boldsymbol{X},t))\cdot\boldsymbol{n}_{e,K}v_h(\boldsymbol{X})\mathrm{d}\Gamma-\int_K\boldsymbol{f}(\boldsymbol{U}_h(\boldsymbol{X},t))\cdot\nabla v_h(\boldsymbol{X})\mathrm{d}\Omega=\int_K\boldsymbol{S}(\boldsymbol{U}_h(\boldsymbol{X},t))v_h(\boldsymbol{X})\mathrm{d}\Omega \tag{3}$$

where

$$\boldsymbol{X}=(x,y)$$
$$\boldsymbol{f}(\boldsymbol{U}(\boldsymbol{X},t))=(\boldsymbol{F}(\boldsymbol{U}(\boldsymbol{X},t)),\boldsymbol{G}(\boldsymbol{U}(\boldsymbol{X},t)))$$

and $\boldsymbol{n}_{e,K}$ denotes the unit outward normal for the edge $e(e=K\bigcap K'\neq\varnothing)$.

Then the flux $\boldsymbol{f}(\boldsymbol{U}_h(\boldsymbol{X},t))\cdot\boldsymbol{n}_{e,K}$ is replaced by the numerical flux $\boldsymbol{h}^{e,K}(\boldsymbol{X},t)$, we obtain

$$\int_K\frac{\partial}{\partial t}\boldsymbol{U}_h(\boldsymbol{X},t)v_h(\boldsymbol{X})\mathrm{d}\Omega+\sum_{e\in\partial K}\int_e\boldsymbol{h}^{e,K}(\boldsymbol{X},t)v_h(\boldsymbol{X})\mathrm{d}\Gamma-\int_K\boldsymbol{f}(\boldsymbol{U}_h(\boldsymbol{X},t))\cdot\nabla v_h(\boldsymbol{X})\mathrm{d}\Omega=\int_K\boldsymbol{S}(\boldsymbol{U}_h(\boldsymbol{X},t))v_h(\boldsymbol{X})\mathrm{d}\Omega \tag{4}$$

The numerical flux is defined as

$$\boldsymbol{h}^{e,K}(\boldsymbol{X},t)=\boldsymbol{h}^{e,K}(\boldsymbol{U}_h(\boldsymbol{X}^{\mathrm{int}(K)},t),\boldsymbol{U}_h(\boldsymbol{X}^{\mathrm{ext}(K)},t)) \tag{5}$$

The value of Eq. (5) at the point $(\boldsymbol{X},t)$ depends on the two values of the approximate solution at $(\boldsymbol{X},t)$. One is the value obtained from the interior of the element K, namely

$$\boldsymbol{U}_h(\boldsymbol{X}^{\mathrm{int}(K)},t)=\lim_{y\to x,y\in K}\boldsymbol{U}_h(y,t)$$

and the other is the value obtained from the exterior of the element K, namely

$$\boldsymbol{U}_h(\boldsymbol{X}^{\mathrm{ext}(K)},t)=\begin{cases}\gamma_h(\boldsymbol{X},t) & \boldsymbol{X}\in\partial\Omega\\ \lim\limits_{y\to x,y\notin K}\boldsymbol{U}_h(y,t) & \boldsymbol{X}\notin\partial\Omega\end{cases}$$

The numerical flux satisfies consistent, monotony, Lipschitz and conservative.

In this paper, the following Local Lax-Friedrichs flux is used

$$\boldsymbol{h}^{e,K}(a,b)=\frac{1}{2}[\boldsymbol{f}(a)\cdot\boldsymbol{n}_{e,K}+\boldsymbol{f}(b)\cdot\boldsymbol{n}_{e,K}-\alpha_{e,K}(b-a)] \tag{6}$$

where $\alpha_{e,K}$ is an estimate of the biggest eigenvalue of the Jacobin $\frac{\partial}{\partial\boldsymbol{U}}\boldsymbol{f}(\boldsymbol{U}_h(\boldsymbol{X},t))\cdot\boldsymbol{n}_{e,K}$ for $(\boldsymbol{X},t)$ in a neighbourhood of the edge e. Moreover, the integrals in Eq. (4) are replaced by quadrature rules

as follows

$$\int_e \boldsymbol{h}^{e,K}(\boldsymbol{X},t)v_h(\boldsymbol{X})\mathrm{d}\Gamma \approx \sum_{l=1}^{L}\omega_l \boldsymbol{h}^{e,K}(\boldsymbol{X}_{el},t)v_h(\boldsymbol{X}_{el})|e| \tag{7}$$

$$\int_K \boldsymbol{f}(\boldsymbol{U}_h(\boldsymbol{X},t))\cdot\nabla v_h(\boldsymbol{X})\mathrm{d}\Omega \approx \sum_{m=1}^{M}\omega_m \boldsymbol{f}(\boldsymbol{U}_h(\boldsymbol{X}_{Km},t))\cdot\nabla v_h(\boldsymbol{X}_{Km})|K| \tag{8}$$

$$\int_K \boldsymbol{S}(\boldsymbol{U}_h(\boldsymbol{X},t))v_h(\boldsymbol{X})\mathrm{d}\Omega \approx \sum_{m=1}^{M}\omega_m \boldsymbol{S}(\boldsymbol{U}_h(\boldsymbol{X}_{Km},t))v_h(\boldsymbol{X}_{Km})|K| \tag{9}$$

Therefore, Eq. (4) is rewritten as

$$\int_K \frac{\partial}{\partial t}\boldsymbol{U}_h(\boldsymbol{X},t)v_h(\boldsymbol{X})\mathrm{d}\Omega + \sum_{e\in\partial K}\sum_{l=1}^{L}\omega_l \boldsymbol{h}^{e,K}(\boldsymbol{X}_{el},t)v_h(\boldsymbol{X}_{el})|e| - \sum_{m=1}^{M}\omega_m \boldsymbol{f}(\boldsymbol{U}_h(\boldsymbol{X}_{Km},t))\cdot\nabla v_h(\boldsymbol{X}_{Km})|K| = \sum_{m=1}^{M}\omega_m \boldsymbol{S}(\boldsymbol{U}_h(\boldsymbol{X}_{Km},t))v_h(\boldsymbol{X}_{Km})|K| \tag{10}$$

For convenient computation, the orthogonal basis functions $\{\varphi_1,\varphi_2,\cdots,\varphi_j\}$ are used inside the rectangular element $[x_{i-1/2},\ x_{i+1/2}]\times[y_{j-1/2},\ y_{j+1/2}]$. Hence, the local mass matrix is diagonal. Then, the expression for the approximate solution $\boldsymbol{U}_h(\boldsymbol{X},t)$ inside the unit K is taken as

$$\boldsymbol{U}_h(\boldsymbol{X},t) = \sum_j \hat{\boldsymbol{U}}_j(t)\varphi_j(\boldsymbol{X}) \tag{11}$$

Set $v_h=\phi_i$ in Eq. (10), we obtain

$$\sum_j \frac{\mathrm{d}\hat{\boldsymbol{U}}_j}{\mathrm{d}t}\int_K \varphi_j(\boldsymbol{X})\varphi_i(\boldsymbol{X})\mathrm{d}\Omega + \sum_{e\in\partial K}\sum_{l=1}^{L}\omega_l \boldsymbol{h}^{e,K}(\boldsymbol{X}_{el},t)\varphi_i|e| - \sum_{m=1}^{M}\omega_m \boldsymbol{f}(\boldsymbol{U}_h(\boldsymbol{X}_{Km},t))\cdot\nabla\varphi_i|K| = \sum_{m=1}^{M}\omega_m \boldsymbol{S}(\boldsymbol{U}_h(\boldsymbol{X}_{Km},t))\varphi_i|K| \tag{12}$$

Make $\boldsymbol{M}_K$ be the mass matrix, for $\forall\ v_h\in V_h$, $\forall\ K\in\Gamma_h$, Eq. (12) can be rewritten in a concise ODEs form as

$$\boldsymbol{M}_K\frac{\mathrm{d}\hat{\boldsymbol{U}}_h(t)}{\mathrm{d}t} = L_h(\hat{\boldsymbol{U}}_h(t),\gamma_h) \tag{13}$$

1.3 Runge-Kutta time discretization

The above system of ODEs is discretized in time with Runge-Kutta method that is third-order accurate and the special steps are shown as follows.

(1) Set $\hat{\boldsymbol{U}}_h^0=P_{V_h}(\hat{\boldsymbol{U}}_0)$, the operator P_{V_h} is the L_2-projection into the finite element space V_h.

(2) For $n=0,\cdots,N-1$, compute $\hat{\boldsymbol{U}}_h^{n+1}$ as follows:

① Set $\hat{\boldsymbol{U}}_h^0=\hat{\boldsymbol{U}}_h^n$.

② For $i=1,\cdots,k+1$, compute the intermediate functions

$$\hat{\boldsymbol{U}}_h^{(i)}=\Big\{\sum_{l=0}^{i-1}\alpha_{il}\hat{\boldsymbol{U}}_h^{(l)}+\beta_{il}\Delta t^n L_h(\hat{\boldsymbol{U}}_h^{(l)},\gamma_h(t^n+d_l\Delta t^n))\Big\}$$

$$\Delta t^n = t^{n+1}-t^n$$

③ Set $\hat{\boldsymbol{U}}_h^{n+1}=\hat{\boldsymbol{U}}_h^{k+1}$.

For more details on the value of α_{il}, β_{il} and d_l, see Ref. [12].

2 NUMERICAL SIMULATIONS

A numerical simulation of the toroidal shock wave focusing in a co-axial cylindrical shock tube is investigated in this paper by using a DG finite element method with third-order accuracy. To validate the numerical method, the shock-tube problem with initial state in Ref. [16] is computed. The comparisons between the computed results and analytical solution show excellent agreements as shown in Fig. 1.

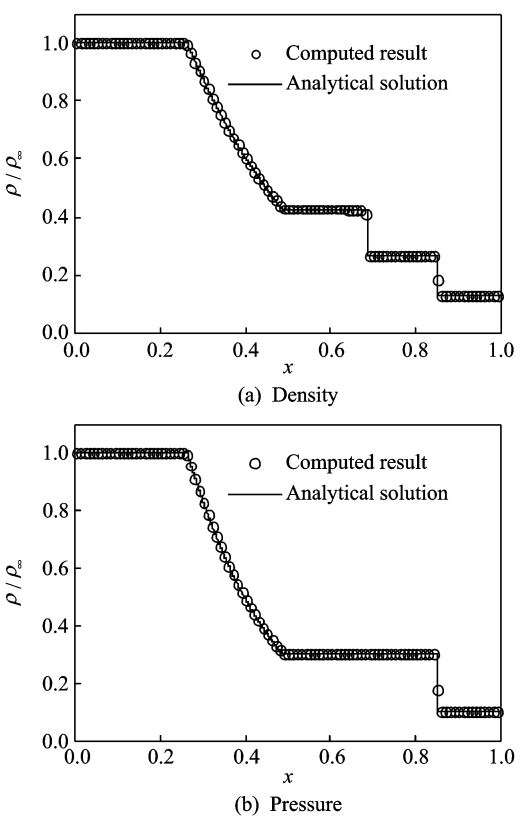

Fig. 1 Comparisons between computed result and analytical solution

Several cases with higher incident Mach numbers varying from 2.0 to 5.0 are computed. A schematic of computational domain, which is $1.0L$ in radial direction and $2.0L$ in axial direction, shown in Fig. 2, is divided into 400×200 grid cells, where $L : D : d = 1 : 0.3 : 0.2$.

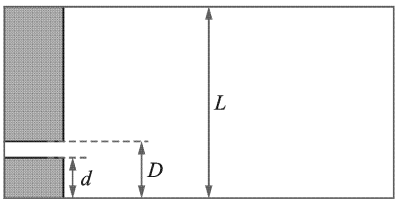

Fig. 2 Computational domain

Fig. 3 shows density contour distributions for incident Mach number $Ma = 3.0$ at different non-dimensional time. The toroidal shock wave, which is discharged from an open end co-axis annular shock tube, diffracts over the backward step be-

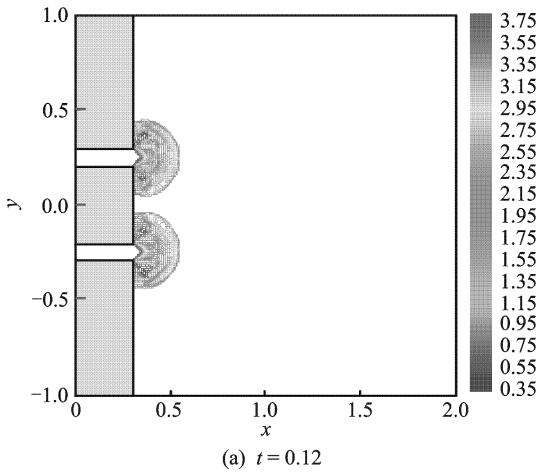

(a) $t = 0.12$

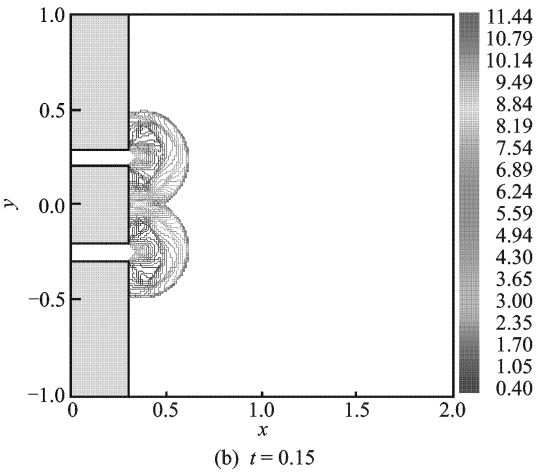

(b) $t = 0.15$

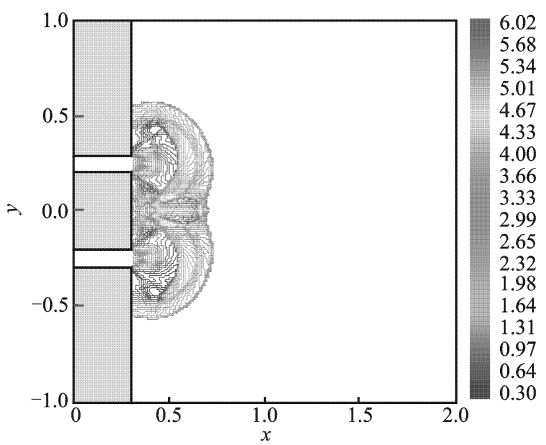

(c) $t = 0.20$

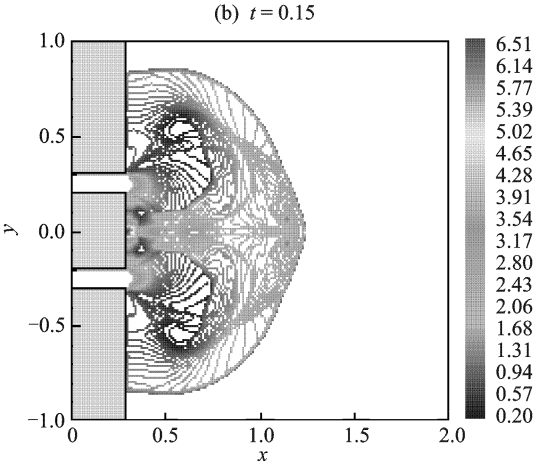

(d) $t = 0.30$

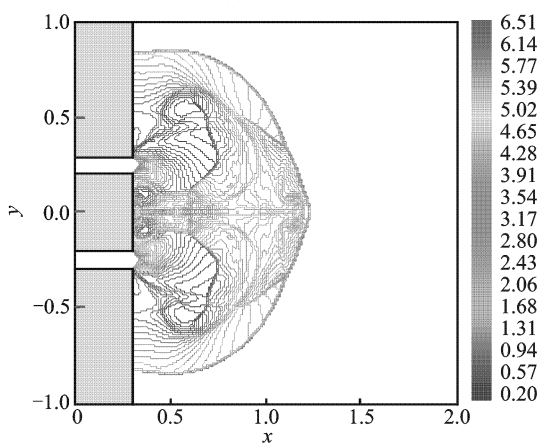

(e) $t = 0.40$

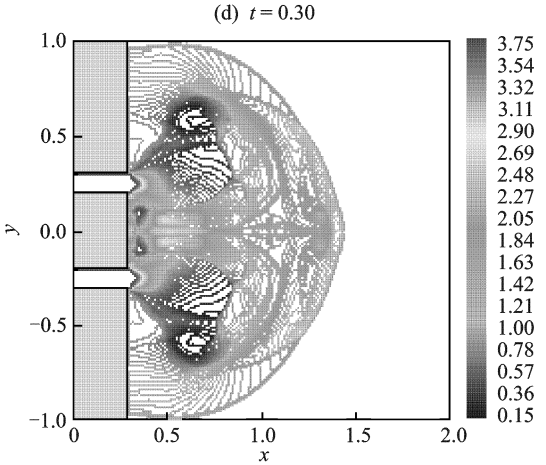

(f) $t = 0.50$

Fig. 3 Density contour distributions at different time ($Ma = 3.0$)

cause of a sudden spread of propagating profile and a vertex ring is formed behind the diffracting shock wave as shown in Fig. 3(a). And then, the diffraction shock wave implodes toward the axis of symmetry and a regular reflection can be observed in Fig. 3(b). Meanwhile, a secondary shock wave is developed because of the local supersonic flow. After focusing, a regular reflection begins to a transitional Mach reflection and a Mach stem is formed, and then develops a spherical Mach reflection, which is called spherical double Mach reflection, as shown in Fig. 3(c). This results from impinging jet generated by shock wave focusing. With the lapse of time, the spherical Mach stem becomes much more convex and there is very complex interaction among shock waves, slip lines, and eddies behind the spherical Mach stem, as shown in Figs. 3(d-f).

Density contour distributions, for incident Mach numbers varying from 2.0 to 5.0 at different non-dimensional time, are shown in Fig. 4. From Fig. 4, it is observed that there are obvious differences in the wave structure. For the case of incident $Ma = 2.0$ as shown in Fig. 4(a), the shock wave reflection with curved Mach stem develops, whose curvature is close to zero and appears nearly planar. Furthermore, some other major flow characters including slip slides and triple point can be captured by computation. With the increase of incident Mach numbers as shown in Figs. 4(b-d), Mach stem is accelerated by stronger impinging jet generated by shock wave imploding and becomes much more convex, further the spherical double Mach reflection is formed. Moreover, vortex ring behind the spherical Mach stem and two triple points can be observed obviously. It is concluded that the incident Mach number of toroidal shock wave plays a vital role in the flow field structure development of shock focusing.

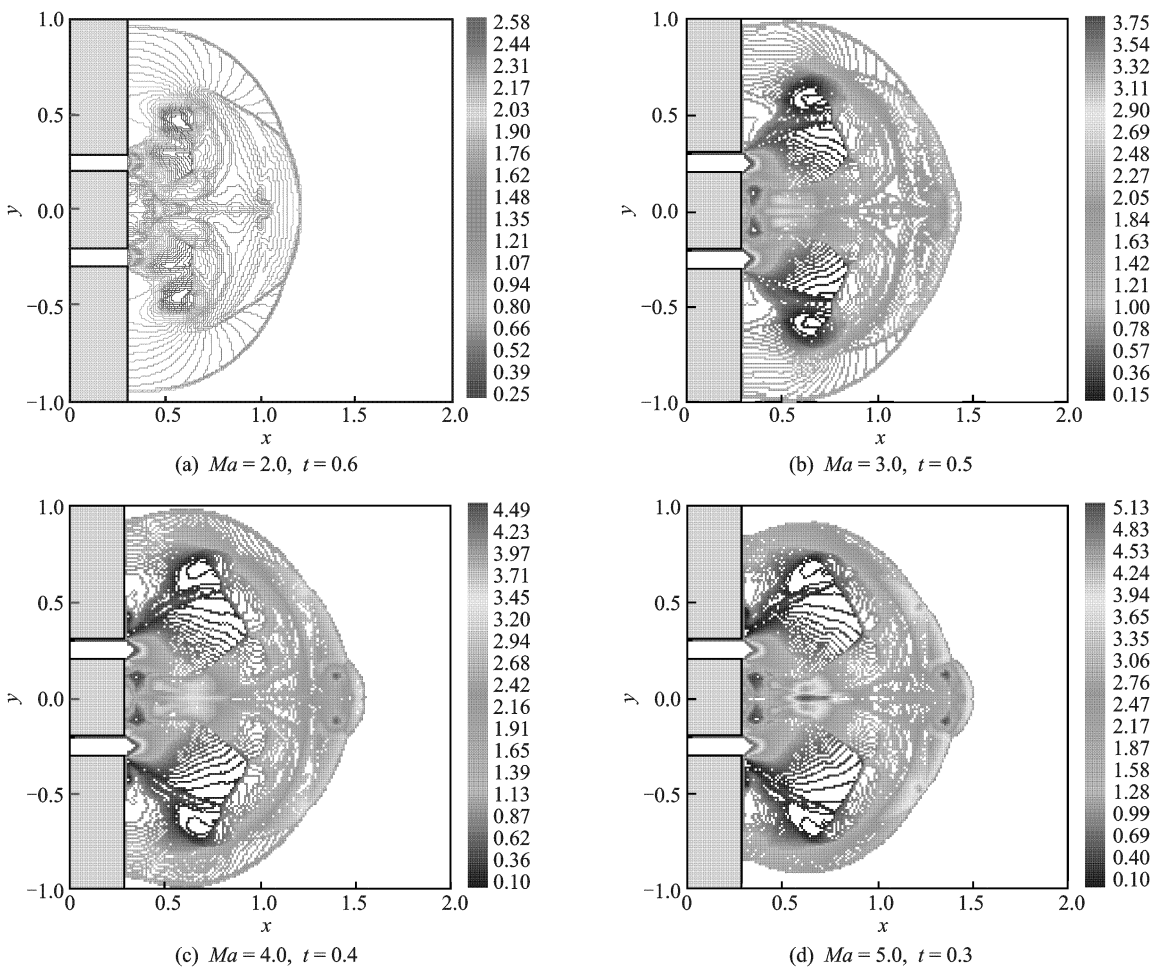

(a) $Ma = 2.0$, $t = 0.6$ (b) $Ma = 3.0$, $t = 0.5$

(c) $Ma = 4.0$, $t = 0.4$ (d) $Ma = 5.0$, $t = 0.3$

Fig. 4 Contour distributions with different incident Mach numbers at different time

Fig. 5 shows the distributions of peak pressure histories along the axis of symmetry for different incident Mach numbers, where p_{max}/p_0 is the ratio of local peak pressure to ambient gas static pressure. From Fig. 5 it can be observed that the peak pressure varies significantly with the increase of shock Mach number. For the cases with $Ma=2.0$, 4.0, the peak pressure increases up to nearly eight times when incident Mach numbers is increased two times. Fig. 6 shows centreline pressure distributions for different incident Mach numbers at a certain time after shock wave focusing, where p/p_0 is the ratio of local gas pressure to ambient gas static pressure. From Fig. 6 it can be observed that the numerical solutions appeared steep gradients near the focusing point, which indicates this method has higher accuracy and resolution near the discontinuous point. Moreover, with the increase of incident Mach number, the peak pressure of shock wave focusing becomes higher.

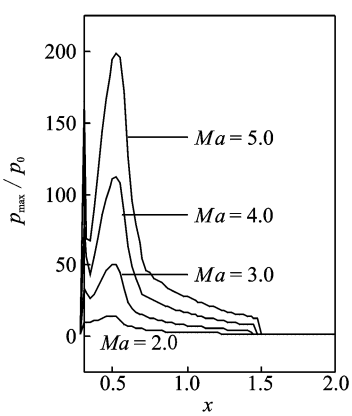

Fig. 5 Peak pressure histories along symmetry axis

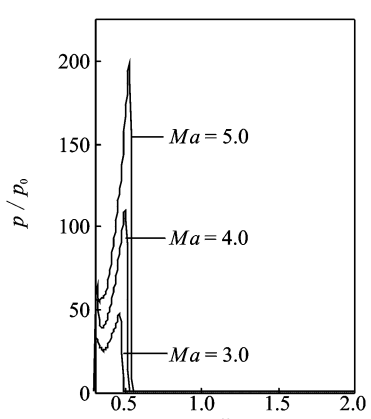

Fig. 6 Pressure distributions of centreline

Fig. 7 shows distributions of peak pressure histories along the axis of symmetry at different grid scales for incident Mach number of $Ma=3.0$. From Fig. 7 it can be observed that the peak pressure nearby the shock focusing point apparently increases with the grid size decreasing. For the case of $\Delta x=\Delta y=1/150$ and $\Delta x=\Delta y=1/300$, the peak pressure increases to nearly 1.5 times when grid size is decreased 2.0 times, which indicates that the computed peak pressure may be less than that of the actual focused pressure.

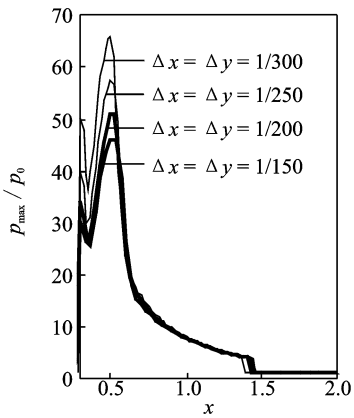

Fig. 7 Distributions of peak pressure histories along symmetry axis at different grid sizes

3 CONCLUSION

A computational study is investigated for the toroidal shock wave focusing in a co-axial cylindrical shock tube using third-order accuracy DG method. Qualitative features of the flow field including the secondary shock wave, vortex ring, triple point, slide line, and spherical double Mach reflection during the process of shock focusing are easily observed in the computed results. And the numerical solutions appear steep gradients near the discontinuous point, which indicates that the method is robust for solving toroidal shock wave focusing problem.

References:

[1] Hosseini S H R, Takayama K. Experimental study of toroidal shock wave focusing in a compact vertical annular diaphragmless shock tube [J]. Shock Waves, 2010, 20(1):1-7.

[2] Teng H, Jiang Z, Han Z, et al. Numerical investigation of toroidal shock wave focusing in a cylindrical chamber [J]. Shock Waves, 2005, 14(4): 299-305.
[3] Babinsky H, Meguro T, Jiang Zonglin, et al. Numerical visualization of shock wave flow in an expanding tube and comparison with experiments [J]. Experimental and Numerical Flow Visualization, 1995, 218: 89-94.
[4] Eliasson V, Apazidis N, Tillmark N, et al. Focusing of strong shocks in an annular shock tube [J]. Shock Waves, 2006, 15(3): 205-217.
[5] Izumi K, Aso S, Nishida M. Experimental and computa-tional studies focusing processes of shock waves reflected from parabolic reflectors [J]. Shock Waves, 1994, 3(3): 213-222.
[6] Dong Gang, Ye Jingfang, Fan Baochun. Experimental and numerical investigation of shock wave focusing and reflection [J]. Chinese Journal of High Pressure Physics, 2006, 20(4):359-364. (in Chinese).
[7] Sod G A. A numerical study of a converging cylindrical shock [J]. J Fluid Mech, 1977, 83:785-794.
[8] Teng Honghui, Jiang Zonglin, Han Zhaoyuan. Numerical investigation of diffraction, focusing and reflection of toroidal shock waves [J]. Acta Mechanic Sinica, 2004, 36(1):9-15. (in Chinese)
[9] Teng Honghui, Zhang Deliang, Li Huihuang, et al. Numerical investigation of detonation direct initiation induced by toroidal shock wave focusing [J]. Explosion and Shock Waves, 2005, 25(6):512-518. (in Chinese)
[10] Teng Honghui, Jiang Zonglin. Gasdynamic characteristics of toroidal shock and detonation wave converging [J]. Science in China: Series G, 2005, 48(6):739-749.
[11] Bokanowski O, Cheng Y, Shu C W. A discontinuous Galerkin solver for front propagation [J]. SIAM Journal on Scientific Computing, 2011, 33(2): 923-938.
[12] Qiu J, Khoo B C, Shu C W. A numerical study for the performance of the Runge-Kutta discontinuous Galerkin method based on different numerical fluxes [J]. J Comp Phy, 2006, 212(2):540-565.
[13] Cheng J, Shu C W. High order schemes for CFD: A review [J]. Chinese Journal of Computational Physics, 2009, 26(5):633-655. (in Chinese)
[14] Chevaugeon N, Xin J, Hu P, et al. Discontinuous galerkin methods applied to shock and blast problems [J]. J Sci Comp, 2005, 22(1):227-243.
[15] Chen Eryun, Ma Dawei, Le Guigao, et al. Numerical simulation of highly underexpanded axisymmetric jet with Runge-Kutta discontinuous galerkin finite element method[J]. Journal of Hydrodynamics: Series B, 2008, 20(5):617-623.
[16] Shu C, Ding H, Chen H Q, et al. An upwind local RBF-DQ method for simulation of inviscid compressible flows [J]. Comput Methods Appl Mech Engrg, 2005, 194(18/20): 2001-2017.

环形激波聚焦流场特性的间断有限元方法

陈二云[1] 赵改平[2] 卓文涛[1] 杨爱玲[1]
(1. 上海理工大学能源与动力工程学院,上海,200093,中国;
2. 上海理工大学医疗器械与食品学院,上海,200093,中国)

摘要:针对环形激波聚焦时产生的高温、高压特性,采用间断有限元方法对环形激波在同轴圆柱形激波管内的聚焦流场进行了数值模拟。为了验证采用方法的有效性,首先对经典激波管问题进行了求解,计算结果与解析解吻合很好。其次,对入射激波马赫数为2.0到5.0的环形激波聚焦流场进行了计算,获得了环形激波在圆柱形激波管内聚焦过程的气动特性。模拟结果表明,采用间断有限元方法能够有效地捕捉激波聚焦过程形成的绕射、反射和聚焦等主要流动特征,而且在聚焦点附近,数值解具有较大的梯度变化,表明该方法对间断解具有较强的捕捉能力。最后比较了网格尺度对聚焦点峰值压力的影响。

关键词:激波聚焦;球面双马赫反射;间断有限元方法
中图分类号:O354.4

(Executive editor: Zhang Huangqun)

基金项目:国家自然科学基金(50976072,51106099,10902070)资助项目;上海市教委重点学科建设基金(J50501)资助项目;上海市教委优秀青年基金(slg09003)资助项目。